

Encapsulation of Prussian Blue Analogues with Conductive Polymers for High-Performance Ammonium-Ion Storage

Qiang Liu, Dongzhi Zhang, Yunting Yang, Yalan Gu, Zhenyan Liang, Wenshu Chen, Yuping Wu, and Linfeng Hu*

Multivalent manganese-based Prussian blue analogues (Mn-PBA) possess multi-electron transfer characteristics and exhibit unique properties for achieving high energy density in ammonium ion batteries (AIBs). However, the irreversible structural collapse and sluggish ionic diffusion kinetics result in inferior rate capability and undesirable lifespan. Herein, guided by theoretical calculations, a series of ultrafine Mn-PBA@conductive polymers core-shell composites through an in situ polymerization and encapsulation strategy are synthesized to solve the above existing issues for Mn-PBA. Among various designed conductive polymers (including the poly-pyrrole (ppy), polyaniline, and poly(3,4-ethylenedioxythiophene)) coated on Mn-PBA, the Mn-PBA@ppy shows the strongest adsorption for ammonium ions and the highest manganese atom removal energy barrier. Acting as the cathode of AIBs, the designed Mn-PBA@ppy exhibits a remarkable high capacity of 72 mAh g⁻¹, a super-stable discharge platform of 0.81 V, and excellent cycling stability of 94% retention for over 300 cycles (0.1 A g⁻¹) with an ultrahigh NH₄⁺ diffusion coefficient of $\approx 1.38 \times 10^{-8} \text{ cm}^2 \text{ s}^{-1}$. This work offers an in situ polymer encapsulation approach to simultaneously enhance the ammonium ion diffusion kinetics and structural stability. More importantly, this organic/inorganic interfacial design can promote the development of cathode materials with rapid diffusion kinetics and excellent cyclic stability.

1. Introduction

Aqueous batteries are gaining considerable interest due to the growing safety concerns surrounding commercial lithium-ion

batteries that use flammable organic electrolytes.^[1] Until now, aqueous batteries commonly use metal ions, such as Li⁺, Na⁺, K⁺, Zn²⁺, and Al³⁺, as charge carriers.^[2-7] However, metal ion batteries suffer from severe dendrite growth behavior during the charge-discharge cycles. Non-metallic charge carriers, such as ammonium ions (NH₄⁺), protons, and hydronium, possess distinctive characteristics, including their lighter molar mass, smaller hydrated ion size, and faster ion diffusion rate compared to traditional metal ion charge carriers.^[8] Especially, in aqueous solution, the NH₄⁺ generates a mildly acidic electrolyte, which can mitigate electrode corrosion and experience less hydrogen evolution compared to protons and hydronium.^[9] Given these advantages, recently, aqueous ammonium ion batteries (AAIBs) have garnered significant attention as a promising next-generation battery technology. To date, a number of electrode materials have been reported for AAIBs, such as metal oxides (e.g., V₂O₅,^[10]

MoO₃,^[11] and MnO_x,^[9] and organic materials (e.g., 3,4,9,10-perylenetetracarboxylic dianhydride^[12] and polyimide^[13]). In general, most of the currently described cathode materials for AAIBs cannot meet the requirements of simultaneously achieving high capacity and stable operating voltage.^[9-12] Undoubtedly, developing new materials that address the above challenge for pursuing high energy density rechargeable AAIBs with satisfied working stability is highly anticipated.

Prussian blue analogues (PBA) of A_{2-x}M[Fe(CN)₆]_{1-y}·zH₂O, where A is an alkali metal and M represents a transition metal, are very appealing candidates for rechargeable battery cathodes owing to their open channel structures that are suitable for ion insertion/extraction.^[14-17] Especially, in recent years, Mn-based PBA have gained intense attention in electrochemical energy storage applications, because they possess two redox-active couples (Mn²⁺/Mn³⁺ and Fe²⁺/Fe³⁺), thus providing a high specific capacity and high operational voltage.^[18] Unfortunately, Mn-PBA typically exhibits high polarizability and inferior cyclic stability as a cathode material due to its poor conductivity, side reactions with the electrolyte, phase transition, and dissolution of Mn element during cycling.^[19]

Various strategies (such as metal oxide coatings,^[20] artificial cathode electrolyte interphase,^[21] and carbon layer coatings^{[22])}

Q. Liu, D. Zhang, Y. Yang, Y. Gu, W. Chen, L. Hu
School of Materials Science and Engineering
Southeast University
Nanjing 211189, P. R. China
E-mail: linfenghu@seu.edu.cn

Z. Liang
School of Chemistry and Chemical Engineering
Qilu University of Technology (Shandong Academy of Science)
Jinan 250353, P. R. China

Y. Wu
School of Energy and Environment
Southeast University
Nanjing 211189, P. R. China

Y. Wu, L. Hu
Z Energy Storage Center
Southeast University
Nanjing 211189, P. R. China

The ORCID identification number(s) for the author(s) of this article can be found under <https://doi.org/10.1002/aenm.202402863>

DOI: 10.1002/aenm.202402863

have been developed to restrain the Mn dissolution and electrode destruction. However, there are many drawbacks for these strategies: I) Poor electrical conductivity of metal oxide coating layer inevitably affects the rate performance of the energy storage battery.^[23] II) Artificial cathode electrolyte interphase still suffers from inferior compatibility with Mn-based cathodes and thus causing an unsatisfactory long-term cycling stability.^[24] The use of carbon materials (including graphene,^[25] graphite layer,^[26] copolymer,^[27] etc.) as coatings for Mn-based cathode materials enables a certain degree of flexibility, which can not only help to relieve the stress of the active material during the ion storage process, but also improve the electrical conductivity of the cathode. Unfortunately, at present, the interface between the carbon layer coating and the Mn-based active material often shows weak connecting or instability characteristic, and the problems of Mn dissolution from the active material still exist, resulting in unsatisfied energy storage performance, especially for the cyclic stability. Therefore, a well-designed interface for the carbon coated Mn-based cathode material with strong and stable interfacial coating layer is very important, but still lacking.^[28]

In this work, we designed an optimal interfacial chemical state in conjugated polymer coated Mn-PBA composite via an in situ polymerization strategy. With the encapsulation of Mn-PBA nanocubes with conductive polymers, the newly formed dense coating layer can effectively promote ion diffusion and prevent Mn atoms dissolution, suggesting the enhanced rate capability and structural stability for the hybrid cathode. In particular, among the conjugated polymer including poly-pyrrole (ppy), polyaniline (PANI), and poly(3,4-ethylenedioxythiophene) (PEDOT), the Mn-PBA@ppy can achieve the highest adsorption energy for ammonium ions and dissolution energy barrier for manganese atoms. Acting as the cathode of ammonium ion batteries, the designed Mn-PBA@ppy exhibits an outstanding energy storage performance, showing a remarkable high specific capacity of 72 mAh g⁻¹, a super stable discharge platform of 0.81 V, and excellent cycling stability of 94% retention for over 300 cycles (0.1 A g⁻¹) with an ultrahigh diffusion coefficient of $\approx 1.38 \times 10^{-8}$ cm² s⁻¹.

2. Results and Discussion

2.1. Theoretical Calculations

To gain a deep understanding on the Mn dissolution suppression effect in the Mn-PBA@conductive polymers, we performed density functional theory (DFT) calculations and investigated the adsorption energies of ammonium ions and the dissolution energy barriers of Mn atoms at the interface. Interestingly, DFT calculations reveal that the adsorption energy of ammonium ions onto Mn-PBA@ppy (4.86 eV) is evidently higher than that for the bare Mn-PBA (3.87 eV), Mn-PBA@PANI (4.52 eV), and Mn-PBA@PEDOT (4.32 eV) (Figure 1a and Table S1, Supporting Information). This difference confirms the effect of dense coating layer in Mn-PBA@conductive polymers, which enables the efficient transport for electrons and ions, thereby promoting fast electrochemical redox kinetics. The calculated energy barriers (E_b) for Mn atoms removed from the interface further reveal the reason of the suppression effect of Mn dissolution in the Mn-PBA@conductive polymers. Results show that the

E_b in bare Mn-PBA is merely 5.79 eV, making the removal of Mn atoms relatively simple. However, when Mn atoms dissolve from Mn-PBA@conductive, a substantially higher energy barriers of 10.62, 8.79, and 7.06 eV, respectively, are required in Mn-PBA@ppy, Mn-PBA@PANI, and Mn-PBA@PEDOT, respectively (Figure 1b; Figures S1 and S2, Supporting Information). The theoretical calculations presented above indicates that the coating of a conductive polymer can enhance the adsorption energy for ammonium ions and the dissolution energy barrier for Mn species from the PBA lattice. The suppression effect of Mn dissolution during the electrochemical NH₄⁺ insertion/extraction in PBA lattice originated from this dissolution energy barrier regulation is further schematically illustrated in Figure 1c. In the case of Mn-PBA, Mn dissolution into the electrolyte occurs through the cathode/electrolyte interface during the cycling process because of the disproportionation reaction of Mn³⁺ that aggravates the dissolution of Mn.^[29] In contrast, for Mn-PBA@conductive polymers, the dissolution of Mn from the crystal is effectively suppressed due to the dense conductive polymer coating layers encapsulated Mn-PBA.^[30,31]

2.2. In Situ Polymer Encapsulation

We then started our experimental study by synthesizing the as-designed Mn-PBA sample and Mn-PBA@ppy, Mn-PBA@PANI, and Mn-PBA@PEDOT composites. X-ray diffraction (XRD) experiments were conducted to study the crystal structures of these prepared Mn-PBA based composites (Figure 2a,b; Figure S3 and Table S2, Supporting Information). Results indicate that the Mn-PBA@ppy, Mn-PBA@PANI, and Mn-PBA@PEDOT retain the characteristic cubic structure of PBA (with a space group of *Fm* $\bar{3}$ *m* and lattice parameters of $a = b = c = 10.09, 10.50, 10.15$ Å, respectively). The Fourier transform infrared (FTIR) spectra of Mn-PBA, Mn-PBA@ppy, Mn-PBA@PANI, and Mn-PBA@PEDOT are depicted in Figure 2d and Figure S4 (Supporting Information). The peak observed at 2070–2150 cm⁻¹ can be attributed to the stretching vibration mode of C≡N bond ($\nu_{C\equiv N}$) located between Mn²⁺ and Fe³⁺ ions.^[32] The peak at 3422 cm⁻¹ corresponds to the stretching vibration mode of the O–H bond (ν_{O-H}), and the peak at 1615 cm⁻¹ stands for the O–H bending mode (δ_{O-H}) of water molecules adsorbed on the sample surface.^[33] The Raman spectra in Figure 2e show that the peaks near 1370 and 1530 cm⁻¹ gradually appear (the two peaks correspond to the D and G bands of graphite), demonstrating the polymer layers are successfully coated for the Mn-PBA@ppy, Mn-PBA@PANI, and Mn-PBA@PEDOT materials.^[34] All of the Mn-PBA based samples exhibit two vibration peaks between 2030 and 2140 cm⁻¹, indicating that the iron cations with carbon coordination exhibit Fe³⁺, while the nitrogen coordinated cations of Mn^{2+/3+}.^[35] The interaction forces between several polymers and Mn-PBA were analyzed using the X-ray photoelectron spectroscopy (XPS) data. Figure S5 (Supporting Information) demonstrates the negative shift of Mn 2p_{1/2} and Mn 2p_{3/2} peaks of Mn-PBA@ppy ($\Delta E = 0.44$ and 0.32 eV, respectively), Mn-PBA@PANI ($\Delta E = 0.34$ and 0.27 eV, respectively), Mn-PBA@PEDOT ($\Delta E = 0.44$ and 0.32 eV, respectively) compared to that of bare Mn-PBA, indicating increased electron density at the Mn atoms provided by conductive polymers and manganese form ionic bond.^[36]

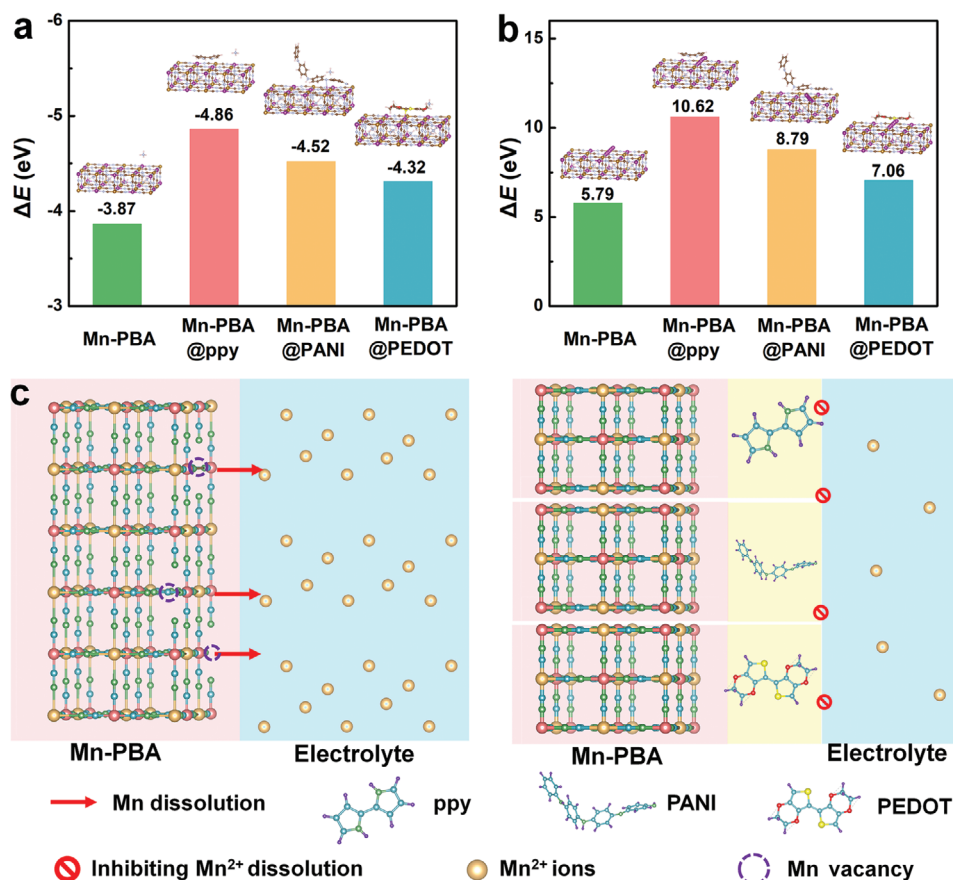


Figure 1. a) Calculated adsorption energies for the ammonium ions on Mn-PBA, Mn-PBA@ppy, Mn-PBA@PANI, and Mn-PBA@PEDOT, respectively. The insets in (a) illustrate the evolution of ammonium ions inserted into bare Mn-PBA, Mn-PBA@ppy, Mn-PBA@PANI, and Mn-PBA@PEDOT, respectively. b) Calculated energy barriers of Mn atoms removed from the interface of Mn-PBA, Mn-PBA@ppy, Mn-PBA@PANI, and Mn-PBA@PEDOT, respectively. The insets in (b) illustrate the evolution of Mn dissolution Mn-PBA, Mn-PBA@ppy, Mn-PBA@PANI, and Mn-PBA@PEDOT, respectively. c) Schematics of Mn dissolution in Mn-PBA and the suppression effect induced by dense conductive polymer coating layers in the Mn-PBA@conductive polymers.

The contact angle tests were performed to evaluate the wettability of the materials, which is an important character for achieving high energy storage performance in aqueous battery systems (Figure 2f). Mn-PBA exhibits a contact angle of 13°, indicating its hydrophilic property. Upon incorporating polymer with Mn-PBA, the contact angles of Mn-PBA@ppy, Mn-PBA@PANI, and Mn-PBA@PEDOT are measured as 27°, 23°, and 19°, respectively. These values represent a small increase as compared to the contact angle of Mn-PBA, however, all the Mn-PBA@conductive polymer samples behave hydrophilic, which will enable the fast and entirely wettability for the aqueous electrolytes. We then studied the morphology and microstructure of the obtained representative Mn-PBA@ppy sample. The transmission electron microscopy (TEM) (Figure 2g) and Field-emission scanning electron microscopy images (Figure S6, Supporting Information) reveal the highly uniform nano-cubic shape with an average size of ≈250 nm for the Mn-PBA@ppy. Figure 2h exhibits the selected area electron diffraction (SAED) pattern along the [001] zone axis of the Mn-PBA@ppy nanocube. Furthermore, the high-resolution TEM (HRTEM) image (Figure 2i) displays a well-ordered crystal lattice with a *d*-spacing of 0.37 nm, which can be

assigned to the (220) planes of Mn-PBA@ppy. This pattern serves as evidence for the monocrystalline structure in the observed individual particle of Mn-PBA@ppy. One can clearly distinguish the ppy coating layer with a thickness of ≈4.3 nm (marked by yellow lines) outside the Mn-PBA nanocubics, demonstrating the successful formation of a “ppy shell/Mn-PBA core” structure. Additionally, the TEM coupled energy dispersive spectrum (EDS) mapping results in Figure 2j–n confirm the homogeneous distribution of Mn, Fe, C, and N elements in the Mn-PBA@ppy sample. These features collectively indicate the successful preparation of a high-quality Mn-PBA@conductive polymer (including ppy, PANI, and PEDOT) samples.

2.3. Ammonium-Ion Storage Behavior

To validate the theoretical investigations of the interfacial dense coating layers on the kinetics, capacity, and dissolution of Mn, we then studied the electrochemical properties of the prepared samples for ammonium ion storage. Through the galvanostatic charge–discharge (GCD) curves (Figure 3a) and *dQ/dV* profiles

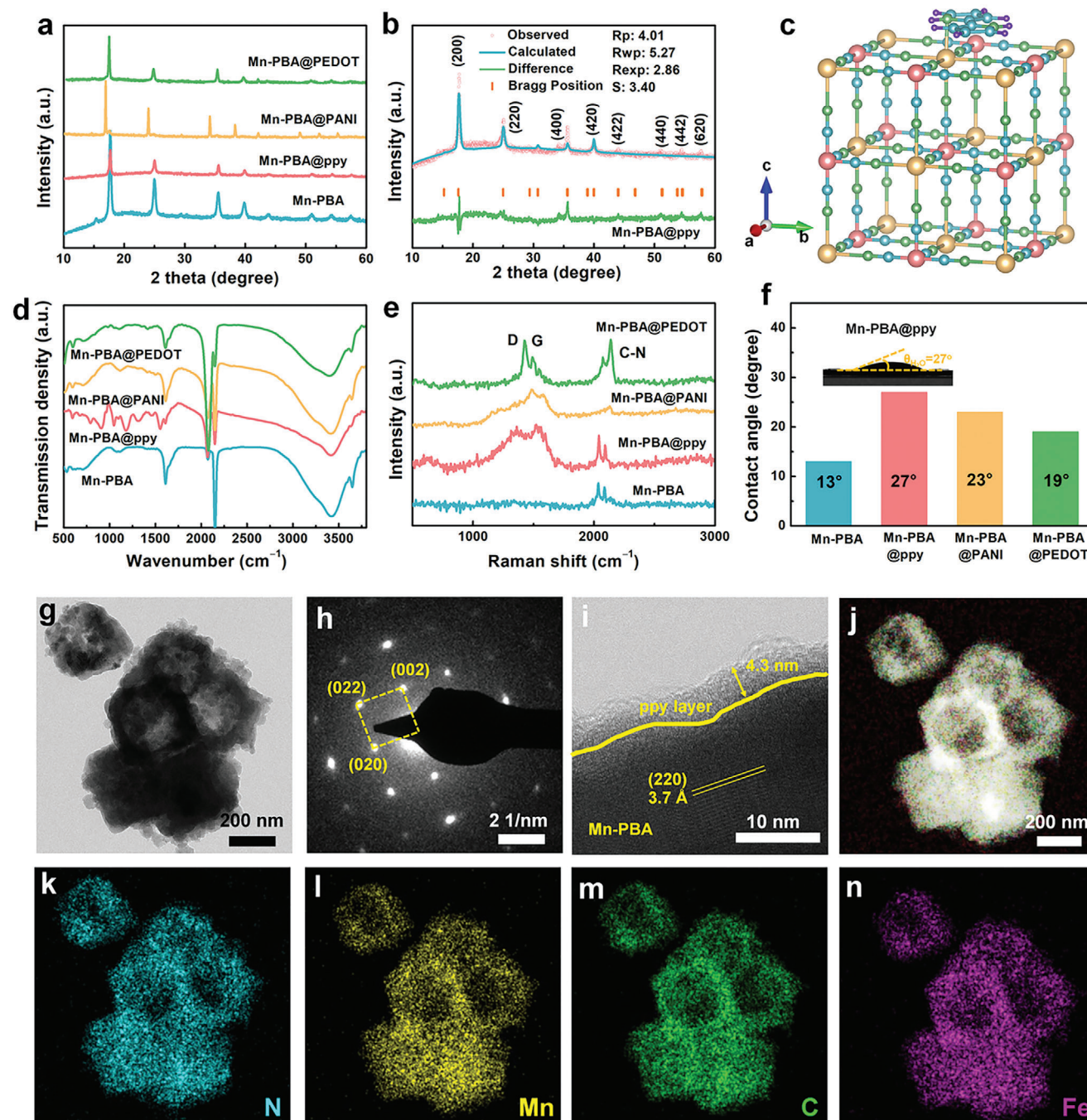


Figure 2. a) XRD patterns of the prepared Mn-PBA, Mn-PBA@ppy, Mn-PBA@PANI, and Mn-PBA@PEDOT samples. b) Rietveld refinement of the XRD pattern and c) crystal structure of Mn-PBA@ppy. d) FTIR spectra, e) Raman spectra, and f) contact angle results of Mn-PBA, Mn-PBA@ppy, Mn-PBA@PANI, and Mn-PBA@PEDOT, respectively. g–n) The TEM image, HRTEM image, SAED pattern, and EDS-mapping results of Mn-PBA@ppy.

(Figure 3b), it is observed that Mn-PBA exhibits a redox potential difference (ΔE) of 0.18 V during the first cycle, which is significantly higher than those of Mn-PBA@conductive polymers, especially for Mn-PBA@ppy (0.12 V). This indicates that the conductive polymer coatings result in a low polarization potential difference, allowing for highly reversible electrochemical reactions. The combination of a stable charge/discharge potential plateau (0.81 V) and remarkable high specific capacity (72 mAh g^{-1}) en-

able the superior energy density compared with some other recently reported cathode materials^[12,37–42] (Figure 3c and Table S2, Supporting Information), making the Mn-PBA@ppy material as a promising candidate for ammonium-ion battery cathodes. Rate capability and long-term cycling stability are crucial factors for evaluating rechargeable battery performance. In terms of rate performance (Figure 3d), the prepared Mn-PBA and Mn-PBA@conductive polymers initially show similar capacities at

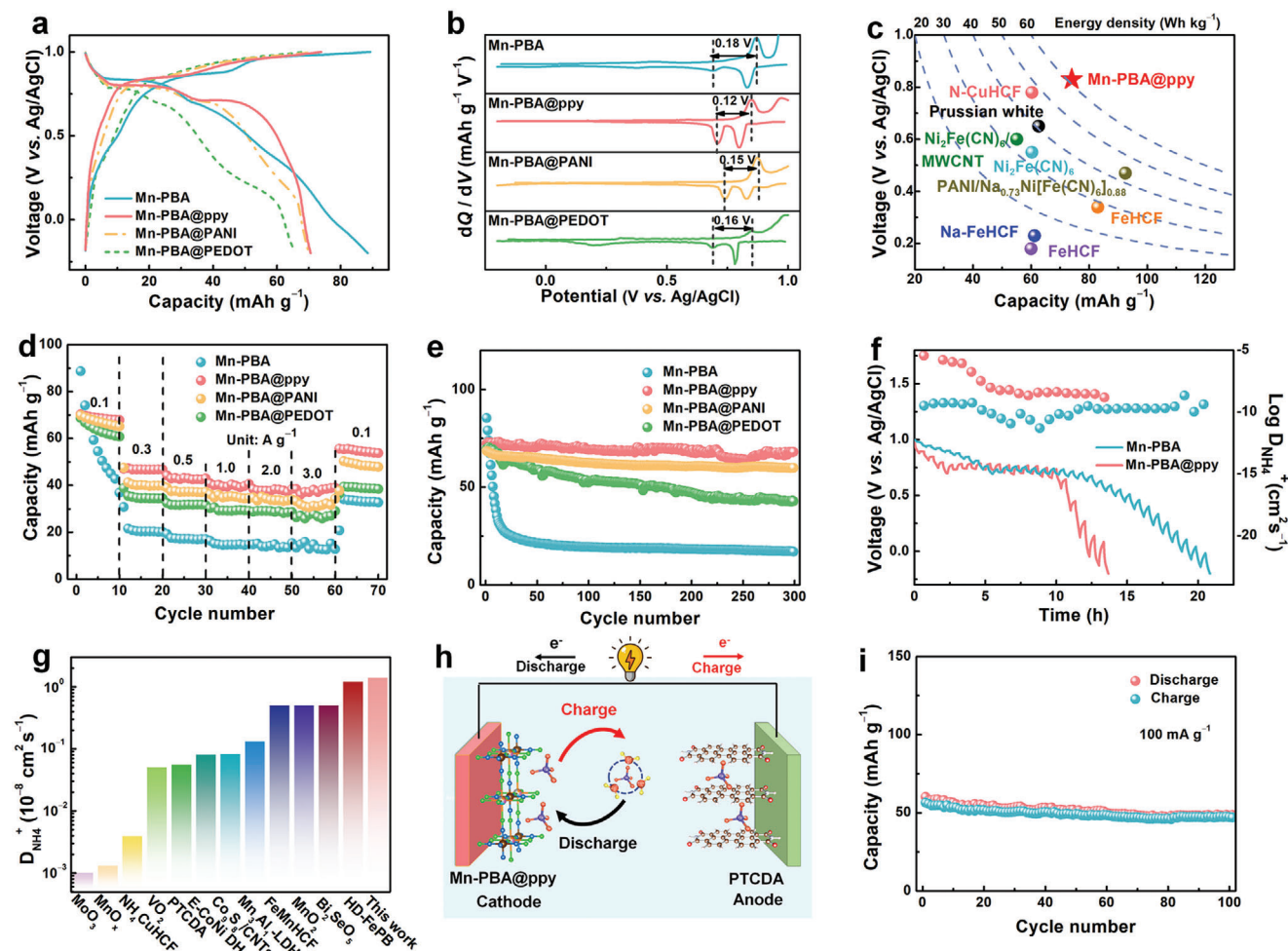


Figure 3. a) GCD profiles at 0.1 A g^{-1} . b) The corresponding dQ/dV curves converted from (a). c) A comparison of the discharge voltage plateaus and specific capacities between our Mn-PBA@ppy nanocubes and some previously reported representative cathodes for aqueous ammonium battery.^[12,37–42] d) Rate performance and e) long-term cycling performance of Mn-PBA, Mn-PBA@ppy, Mn-PBA@PANI, and Mn-PBA@PEDOT cathodes. f) GITT profiles in the second cycle and the calculated ammonium ions diffusion coefficients. g) A comparison of the NH_4^+ diffusion coefficients between our Mn-PBA@ppy composite and some previously reported cathode materials for aqueous ammonium battery.^[43–54] h) A schematic of the assembled Mn-PBA@ppy//PTCDA ammonium ion full battery. i) Cycle performance of the assembled full battery at 0.1 A g^{-1} .

0.1 A g^{-1} , however, the Mn-PBA@ppy sample exhibits competitive reversible capacity of 39 mAh g^{-1} with a steady GCD curve even at a high current density of 3.0 A g^{-1} , surpassing those of the Mn-PBA (13 mAh g^{-1}), PBA@PANI (33 mAh g^{-1}), and Mn-PBA@PEDOT (28 mAh g^{-1}). Long-term cycling test conducted at a current density of 0.1 A g^{-1} reveals the exceptional high cycling stability for our Mn-PBA@ppy cathode, which exhibits a remarkable high-capacity retention of 94% after 300 cycles. This performance stands in stark contrast to the unsatisfied stability of Mn-PBA, PBA@PANI, and Mn-PBA@PEDOT, which achieve only 20%, 87%, and 61% retentions, respectively, under the same conditions (Figure 3e).

The evaluation of the electrochemical properties of the composite is affected by whether the coating layer has ion storage capacity. Accordingly, the ammonium ion storage test was conducted on pure ppy. As shown in Figure S7 (Supporting Information), the pure ppy cathode in $2 \text{ M NH}_4\text{OTf}$ electrolyte almost show no capacity ($\approx 6 \text{ mAh g}^{-1}$) on energy storage at

0.1 A g^{-1} . On the other hand, the amounts of conductive polymers are also an important factor affecting the electrochemical performance, so we tested the ammonium ion storage performance of different amounts of ppy (Figure S8, Supporting Information). We label the drops of pyrrole monomer (100 and 200 μL) as Mn-PBA@ppy1 and Mn-PBA@ppy2. Long-term cycling tests conducted at a current density of 0.1 A g^{-1} reveal that our Mn-PBA@ppy1 and Mn-PBA@ppy2 cathode exhibit exceptional cycling stability, retaining a remarkable capacity of 94% and 91% after 300 cycles. However, the excessive coating content of ppy resulted in an initial capacity of only 43 mAh g^{-1} for Mn-PBA@ppy2, which is much lower than for Mn-PBA@ppy1 (72 mAh g^{-1}). The aforementioned results demonstrate that Mn-PBA@ppy1 is the optimal selection for high-capacity and stable ammonium storage.

Detailed electrochemical analysis was then conducted to elucidate the internal kinetics behind the competitive ammonium ion storage performance for our best-performed Mn-PBA@ppy

cathode. The kinetics of ammonium-ion diffusion was first assessed utilizing the galvanostatic intermittent titration technique (GITT), as shown in Figure 3f. Strikingly, an exceptionally high diffusion coefficient for ammonium ions of $\approx 1.38 \times 10^{-8} \text{ cm}^{-2} \text{ s}^{-1}$ was observed in Mn-PBA@ppy, far surpassing that of the pristine Mn-PBA cathode ($\approx 5.62 \times 10^{-10} \text{ cm}^{-2} \text{ s}^{-1}$) as well as certain previous studies^[43–54] (Figure 3g). This finding serves as a confirmation of the significant improvement in electrochemical ion storage kinetics achieved through the implementation of our optimized in situ polymer encapsulation strategy. We have tested the electrochemical impedance to study the dynamics of the electrode material. The Nyquist plot includes the high-frequency region which corresponds to the charge transfer resistance (R_{ct}) and the low-frequency region represents the signal of ion diffusion resistance. The R_{ct} of Mn-PBA@ppy (18.20 Ω) is smaller than that of Mn-PBA (24.92 Ω), suggesting Mn-PBA@ppy has a superior electron conductivity (Figure S9 and Table S4, Supporting Information).

Cyclic voltammetry (CV) curves obtained with different scan rates provide valuable insights into the energy storage behaviors and mechanisms and enable the determination of energy storage capacity contribution ratios for ammonium ion storage by analyzing the relationship between peak current densities and scan rates (Figure S10, Supporting Information). The b values of four different peaks A–D of 0.99, 0.79, 0.73, and 0.87 can be derived for the peak A to peak D of the four primary peaks, respectively, indicating capacitive-effect is the predominant contribution for ammonium-ion storage in the Mn-PBA based cathodes. For the Mn-PBA@ppy sample, the proportion of capacitive-controlled capacity ranges from 63% to 88% as the scan rate increases from 0.2 to 1.0 mV s^{-1} , which are much higher than that of Mn-PBA (ranging from 28% to 58%). This indicates an increase in the capacitive contribution with the coating of poly-pyrrole, highlighting the enhanced capacitive behavior of Mn-PBA@ppy.

To evaluate the practical application potential, we endeavor to construct a full battery based on our Mn-PBA@ppy cathode (Figure 3h). The Mn-PBA@ppy//3,4,9,10-perylenetetracarboxylic dianhydride (PTCDA) full battery was assembled, with commercial PTCDA selected as the anode material due to its suitable reduction potential and two-electron reaction (Figure S11a, Supporting Information). The CV curves obtained during the initial three cycles exhibit no significant changes, displaying two prominent oxidative peaks at 0.88/1.28 V and well-defined reductive peaks at 0.41/1.23 V in the scan, which suggest the excellent reversibility for the assembled full battery (Figure S11b, Supporting Information). The GCD profile verifies a specific capacity of 56 mAh g^{-1} (based on the total active mass of cathode and anode materials) for the constructed full battery (Figure S11c, Supporting Information). The rate performance of the Mn-PBA@ppy//PTCDA full battery reveals reversible capacities ranging from 53 to 28 mAh g^{-1} as the current density increases from 0.1 to 5.0 A g^{-1} (Figure S11d, Supporting Information). Upon returning to 0.1 A g^{-1} , the capacity rapidly recovers to 46 mAh g^{-1} , indicating a decent high-rate tolerance of the full battery. In terms of long-term cycling performance, the Mn-PBA@ppy//PTCDA full battery demonstrates an impressive cycle life exceeding 100 cycles at 0.1 A g^{-1} . It also exhibits a satisfactory capacity retention of 84% and a high Coulombic efficiency of 94% (Figure 3i).

2.4. Mechanism of Stability Enhancement

To further elucidate the ammonium ion storage mechanism for the Mn-PBA@ppy, we conducted ex situ XRD analysis to investigate the structural changes during the initial galvanostatic discharge/charge/discharge cycles. As a comparison, we first studied the phase evolution of the cubic Mn-PBA (Figure 4a–c). The diffraction peak at 17.05°, representing the (200) planes of the cubic phase of Mn-PBA, progressively becomes weakened from the initial state of A to the 0.6 V discharged state of B and disappears entirely at the fully discharged state of C (Figure 4b,c), indicating an insertion/extraction mechanism for NH_4^+ ion storage. Simultaneously, a new diffraction peak emerges at 17.36° at the fully discharged state of C, corresponding to the tetragonal phase of Mn-PBA. Upon charging the battery from the –0.2 V charged state of D to the 1.0 V charged state of G, the diffraction peaks of Mn-PBA transform entirely from the tetragonal phase to a cubic phase. However, upon full discharge of Mn-PBA to –0.2 V charged state of J in the second cycle, the diffraction peaks indicate a mixture of tetragonal and cubic phases, indicating an irreversible phase transition for the cathode. In contrast, the Mn-PBA@ppy show quite different phase evolutions during the cycles (Figure 4d–f). The ex situ XRD patterns reveal that the (200) diffraction peak shifts to higher 2θ degrees from the pristine state of A to the discharged –0.2 V state of C, and then gradually returns to lower degrees during the charging process to 1.0 V (Figure 4e,f). In the subsequent cycle, the phase transition from cubic to tetragonal structure cannot be observed in our Mn-PBA@ppy sample, which returns to the cubic phase after the initial charge is completed. This phenomenon has also been observed in the previously work reported by other groups.^[55] The ppy coating can suppress the volume changes during the charge/discharge process and effectively alleviate the internal stress of the PBA lattice, which might be responsible for the suppression of the phase change. Overall, the ex situ XRD characterizations support a feasible energy storage mechanism of ammonium-ion insertion/extraction within the Mn-PBA@ppy framework, maintaining its overall structure without phase transformation during the electrochemical charge/discharge process.

We then performed ex situ XPS characterizations to verify the reversible electrochemical energy storage mechanism of ammonium ion insertion/extraction within the 3D open skeleton crystal structure of Mn-PBA@ppy (Figure 4g,h). Figure 4g displays the Mn 2p XPS spectra and the deconvolution results at different discharged/charged states (marked in Figure 4d) of Mn-PBA@ppy. In the discharge process from the pristine state of A to the discharged –0.2 V state of C, the intensity of the Mn^{3+} peak at 642.5 eV decreases, while the intensity of the Mn^{2+} peak at 641.1 eV increases, indicating the reduction of Mn^{3+} to Mn^{2+} due to the insertion of ammonium ions into Mn-PBA@ppy.^[56] Conversely, in the charge process from the charged –0.2 V state of C to the charged 1.0 V state of E, the intensity of the Mn^{3+} peak increases, accompanied by the weakening of the Mn^{2+} peak. The characteristic binding energies (E_{B}) of 397.7 and 400.0 eV correspond to the metal-N and pyrrolic N of the $[\text{Fe}(\text{CN})_6]^{3-}$ complex, respectively.^[57] Then, a new peak of –N–H– at 401.8 eV emerges in the discharged state of B and intensifies from the discharged state of B to the fully discharged state of C, indicating the NH_4^+ ions are inserted into the Mn-PBA@ppy host during the

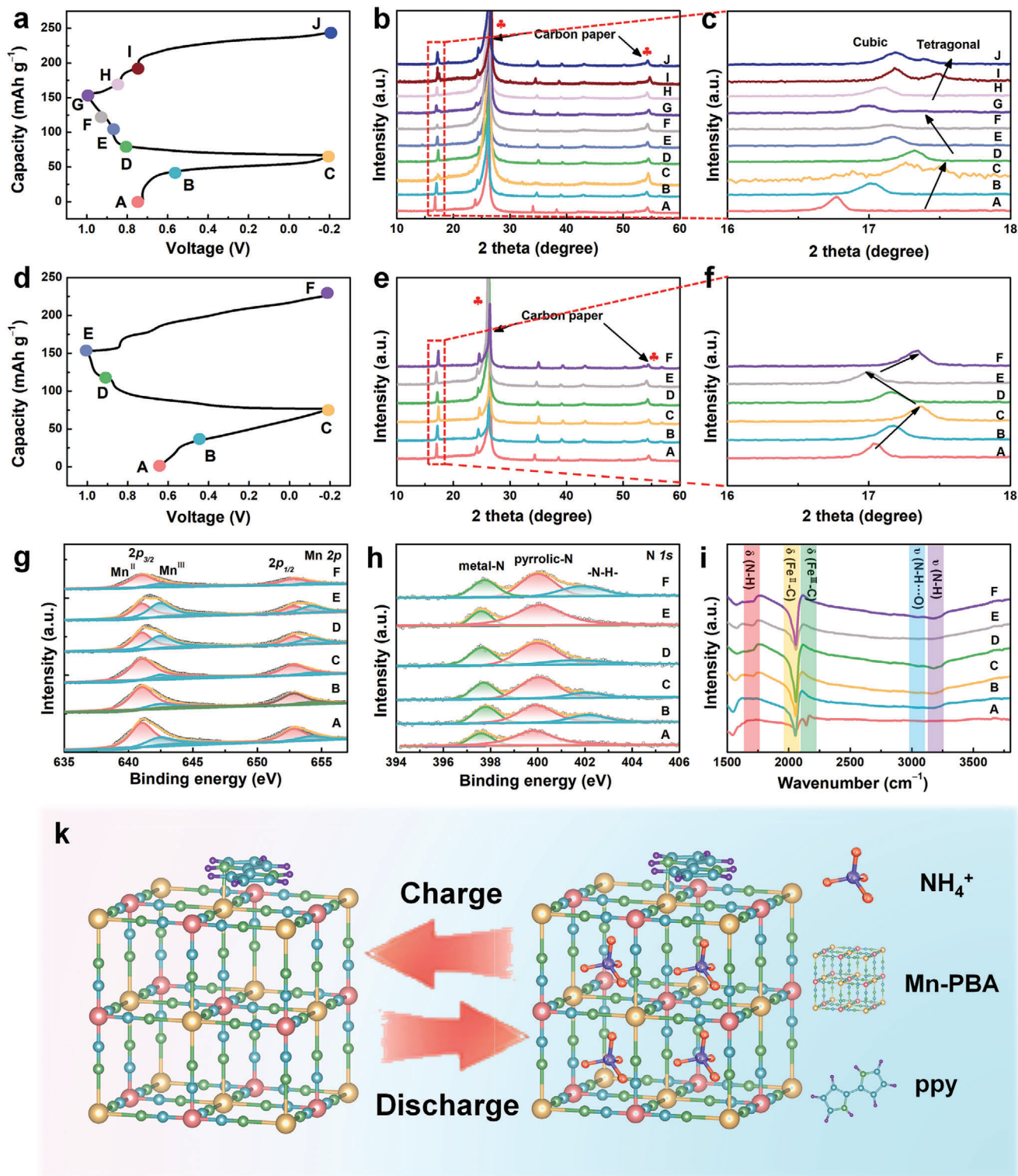


Figure 4. GCD curves of a) Mn-PBA and d) Mn-PBA@ppy cathodes to marked out the traced states. Ex situ XRD patterns of b,c) Mn-PBA and e,f) Mn-PBA@ppy. Ex situ XPS spectra for g) Mn 2p, h) N 1s orbitals, and i) ex situ FTIR spectra of the Mn-PBA@ppy cathode sampled at different charge–discharge states from A to F. k) A schematic illustration of the ammonium-ion storage mechanism in the Mn-PBA@ppy host.

discharge process.^[58] Subsequently, this —N—H— peak intensity weakens from the fully discharged state of C to the fully charged state of E and becomes strengthened from the fully charged state of E to the fully discharged state of F, suggesting the highly reversible ammoniation and de-ammoniation process for the Mn-PBA@ppy host material (Figure 4h).

Ex situ FTIR spectra provide further evidence of hydrogen bond formation of the Mn-PBA@ppy cathode during the ammoniation/de-ammoniation cycles (Figure 4i). The observed peaks at 1410 and 3180 cm^{-1} are attributed to the vibration modes of $\delta_{(\text{HNH})}$ and $\nu_{(\text{NH})}$, respectively, indicating the entry of NH_4^+ into the Mn-PBA@ppy lattice.^[59] Specifically, the intensities of these peaks gradually increase from the pristine state of A to the fully charged state of C, suggesting that the ammonium ions are inserted into the cathode through hydrogen bonding with the M—N (M = Fe and Mn). After that, they decrease from the fully charged state of C to the charged 0.91 V state of D and completely disappear at the charged 1.0 V state of E, indicating the de-ammoniation process is accompanied by the breaking of hydrogen bonds. The presence of the N—H signal confirms the successful insertion of NH_4^+ ions into the lattice of the Mn-PBA@ppy crystal, which aligns with the findings from the N 1s XPS spectra shown in Figure 4h. The above mechanism investigations indicate that NH_4^+ insertion/extraction occurs reversibly in the Mn-PBA@ppy host (Figure 4k).

It is widely recognized that manganese dissolution is the primary cause of capacity attenuation in manganese-based electrode materials. Therefore, we first studied the change in the physical state of the electrolytes before and after cycling within the Mn-PBA and Mn-PBA@ppy electrodes to assess the manganese dissolution situation. To observe the changes in the electrolyte more clearly, electrochemical tests were conducted using a three-electrode system. The Mn-PBA and Mn-PBA@ppy served as the working electrodes, while activated carbon (AC) and an Ag/AgCl electrode functioned as the counter and reference electrodes, respectively. Evidently, the electrolyte for Mn-PBA@ppy remains colorless and transparent after 300 cycles (Figure 5a), indicating the stability of the cathode material. Whereas, the electrolyte for Mn-PBA undergoes a noticeable color change after only 100 cycles, indicating the dissolution of a certain manganese species. Following prolonged cycling, the electrolyte for Mn-PBA exhibits a deepened yellow color, indicating the increased dissolution of manganese element. To quantify the above observed results and to establish the relationship between Mn dissolution and capacity decline, the electrolytes after various cycles were collected and the concentration of dissolved manganese ions was measured on an inductively coupled plasma optical emission spectrometer. Similar to other manganese-based materials, Mn-PBA experiences significant manganese dissolution, with a Mn concentration of 3.6 mg L^{-1} in the electrolyte after 300 cycles. This dissolution is believed to be responsible for the inferior electrochemical performance of Mn-PBA. In sharp contrast, the manganese dissolution issue in Mn-PBA@ppy is effectively suppressed, with only 0.55 mg L^{-1} of Mn detected in the electrolyte after 300 cycles (Figure 5b). This result demonstrates the excellent chemical stability for the Mn-PBA@ppy sample achieved through the interfacial dense coating layers design. In order to investigate whether phase transition reactions occur during long cycles, the phase structure of the cathode after 5, 50, 100, 150, 200, 250, and 300

cycles is examined (Figure 5c,d). All obtained peaks can be classified to the characteristic peaks of cubic Mn-PBA@ppy and the carbon paper substrates, indicating a robust structural stability of the Mn-PBA@ppy nanocubes during the long-term cycling. TEM observations of Mn-PBA@ppy after 100 and 300 cycles were performed to assess the evolution of their cubic nanocrystal morphologies during the cycling test (Figure 5e,f). The results reveal that the cubic-like morphology of Mn-PBA@ppy is well maintained after 100 and 300 charge/discharge cycles, whereas Mn-PBA undergoes severe morphological disruption (Figure S13, Supporting Information). Furthermore, the TEM coupled EDS mapping results after 100 and 300 charge/discharge cycles show a homogeneous distribution of Mn, Fe, C, and N elements within the nano-cubic morphology for the Mn-PBA@ppy sample (Figure 5g,h), confirming the uniform and stable elemental distribution in the nanocubes after 100 and 300 cycles.

3. Conclusion

In conclusion, we have proposed and optimized an interfacial binding engineering design on Mn-PBA cathode through an in situ polymerization encapsulation strategy. Within the theoretical and experimental screening, we verify that Mn-PBA coated with conductive conjugated polymer of ppy show a stronger adsorption capacity for ammonium ions and a higher energy barrier for the removal of manganese atoms over other investigated samples. Benefiting from these characteristic advantages, the prepared Mn-PBA@ppy demonstrates significantly improved capacity, redox kinetics, and cyclic stability, surpassing those of previously reported ammonium ion battery cathode materials. This methodology ensures an even distribution of the polymer coating layer on the Mn-PBA precursor, facilitating precise control over the coating's stoichiometry and the formation of a thin, uniform, and tightly coating layer. Our insights into interface engineering design hold the promise of facilitating rapid diffusion kinetics and superior cyclic stability for ammonium ion storage. Furthermore, the reported strategy on dense coating layer is expected to be extended to other electrochemical fields, such as electrocatalysis, to enhance the structural stability and electron/ion transport properties, thereby improving the electrochemical performance.

4. Experimental Section

Material Synthesis: Mn-PBA was synthesized via a coprecipitation method followed by an aging process. Detailly, solution A was prepared by dissolving 10 mmol of potassium hexacyanoferrate (III) into 100 mL of deionized water. Solution B was formed by adding 20 mmol of $\text{MnCl}_2 \cdot 4\text{H}_2\text{O}$ into 100 mL of DI water. Then, solution A and solution B were dropwisely added to 200 mL of deionized water under magnetic stirring. After that, a brown sediment was collected centrifugally, washed with deionized water and ethanol, and then dried in a vacuum oven under 60 °C for 24 h. To prepare the Mn-PBA@ppy sample, 0.20 g synthesized Mn-PBA nano-cubes were dispersed in 30 mL of water, followed by adding pyrrole monomer (100 μL) and stirring for 30 min to form a mixed solution. Subsequently, 30 mL FeCl_3 solution (11:9 mole ratio of FeCl_3 to pyrrole monomer) was added dropwisely into the mixed solution while stirring continuously. The in situ oxidative polymerization reaction was then initiated at room temperature and allowed to proceed for 24 h. After then, black Mn-PBA@ppy composites were collected through centrifugation. They were washed several times with ethanol and deionized water

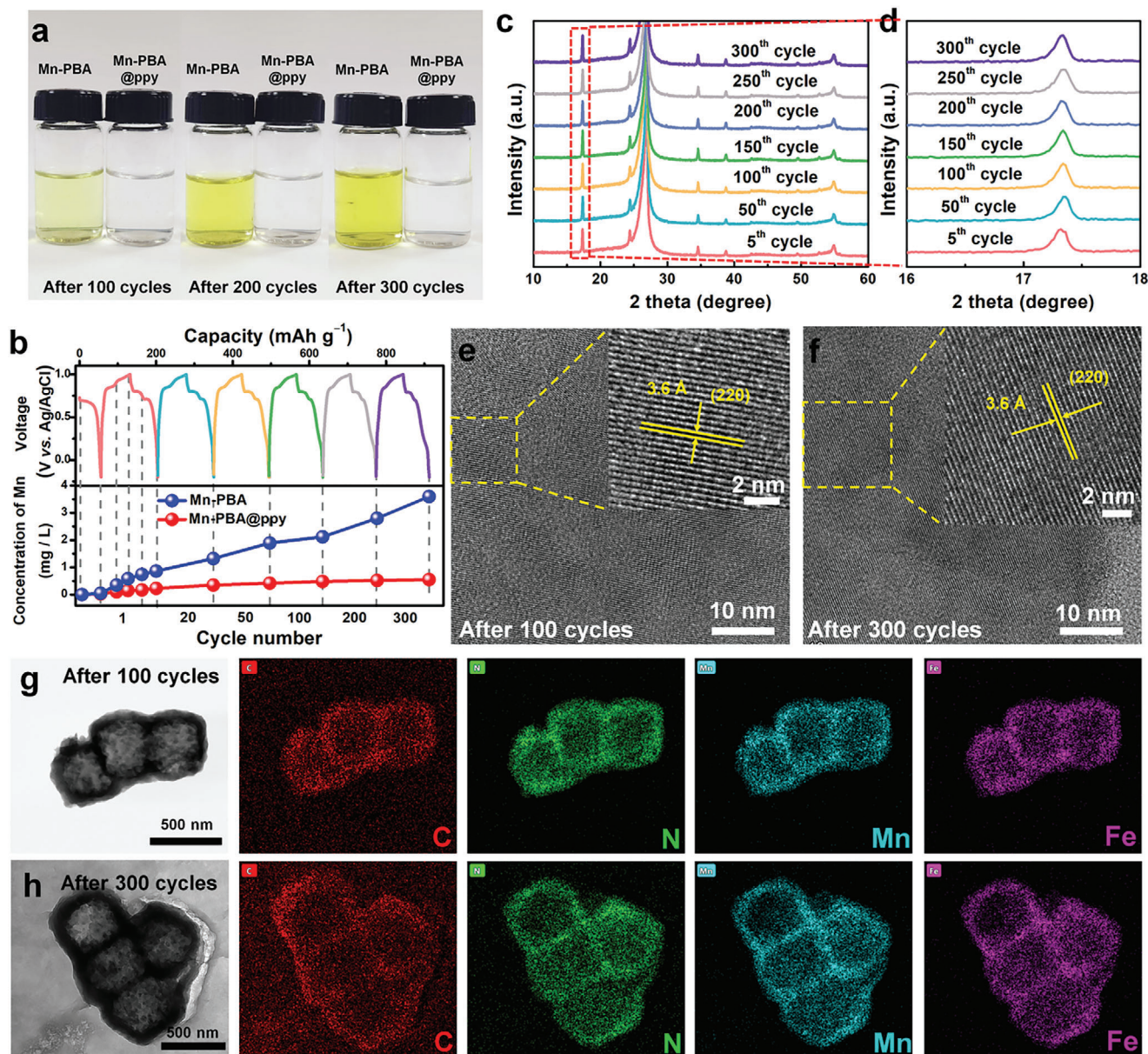


Figure 5. a) Digital images of electrolytes before and after various cycles. b) ICP results of Mn dissolution after different charge/discharge cycles. c, d) XRD patterns of Mn-PBA and Mn-PBA@ppy cathodes after 5, 50, 100, 150, 200, 250, and 300 charge/discharge cycles. e, f) HRTEM images and g, h) EDS mapping results of the Mn-PBA@ppy cathode after 100 and 300 cycles.

and then dried at 60 °C for 24 h. Mn-PBA@PANI and Mn-PBA@PEDOT samples were synthesized following the similar process.^[46,47]

Material Characterization: The crystal structures were studied by XRD (Rigaku Ultima IV diffractometer with Cu K α radiation ($\lambda = 1.5406 \text{ \AA}$)). The morphology and structure of samples were characterized using a TEM (FEI Talos F200X). SAED and EDS (EDS mapping) tests were carried out accompanied with the TEM experiments. The elemental compositions and chemical states of samples were analyzed by XPS (Thermo Scientific Escalab 250Xi). The chemical bonding of the samples was revealed by an FTIR (Bruker TENSOR II). Inductive coupled plasma (ICP) emission spectrometer experiments were conducted on Agilent 5100 to measure the metal element concentrations. A water-based angle contact experiment (JY-82) was developed based on the pressed powder.

Electrochemical Measurement: The Mn-PBA and Mn-PBA@conductive polymer cathodes for aqueous ammonium ions batteries were prepared by mixing Mn-PBA or Mn-PBA@conductive polymers, acetylene black, and polyvinylidene fluoride (PVDF) in a mass ratio of 7:2:1, with the addition of 1-methyl-2-pyrrolidinone, followed by coating onto a carbon paper and drying under vacuum at 80 °C for 12 h. Activated carbon films were utilized as the anodes, which were prepared by mixing the activated carbon, acetylene black and PVDF in a mass ratio of 7:2:1. Then, the slurry was coated onto a carbon paper and dried under vacuum at 80 °C for 12 h. The resulting slurry-coated carbon paper was cut into $\Phi 10 \text{ mm}$ electrodes, and a 2.0 M NH_4Otf electrolyte solution was prepared. Within the prepared electrodes, separator, electrolyte, counter electrode, Swagelok cells were assembled in a three-electrode configuration for electrochemical performance of ammonium ion battery.

The CV and EIS tests were conducted on an electrochemical workstation (CHI660E). The GCD, GITT, and long-term cycling tests were carried out on a LAND battery test system (CT3001A).

Computational Details: DFT calculations were performed using the projector augmented plane-wave method within the Vienna Ab initio simulation package. The generalized gradient approximation was used in the scheme of Perdew–Burke–Ernzerhof to describe the exchange–correlation function. The cut-off energy for plane wave was set to be 480 eV. The energy criterion was set to be 10^{-4} eV in iterative solution of the Kohn–Sham equation. All the structures were relaxed until the residual forces on the atoms have declined to less than 0.05 eV \AA^{-1} . To prevent interaction between periodic units in the vertical direction, a vacuum space of 20 \AA was employed. A Monkhorst–Pack scheme with a k-points mesh of $1 \times 2 \times 1$ was used. The diffusion barrier of adsorbed hydrogen at different adsorption sites were explored by using the nudged elastic band (CI-NEB) method.

Calculation Methods: The calculation method for the capacity contribution was based on the following equation:

$$I_p = C_1\nu + C_2\nu^2 \quad (1)$$

where I_p (A g^{-1}) is the peak current density at different scan rate, ν (mV s^{-1}) is the specific scan rate, and C_1 and C_2 are the corresponding constant factors of the capacity contribution of surface pseudocapacitive effect and battery-type effect, respectively.

With a deformation of the above equation, the specific contribution rate of different internal mechanisms can be solved according to the following equation:

$$\frac{I_p}{\nu^2} = C_1\nu^{-1} + C_2 \quad (2)$$

The diffusion coefficient ($D_{\text{NH}_4^+}$) of ammonium ions can be experimentally calculated by a GITT method in terms of the following equation:

$$D = \frac{4}{\pi\tau} L^2 \left(\frac{\Delta E_s}{\Delta E_t} \right)^2 \quad (3)$$

where D is the diffusion coefficient of ammonium ions, τ is the relaxation time of the current pulse, L is the diffusion length which is approximate to the thickness of coated slurry, and ΔE_s and ΔE_t are the voltage changes produced by the current pulse and the galvanostatic charge/discharge, respectively.

Supporting Information

Supporting Information is available from the Wiley Online Library or from the author.

Acknowledgements

This work was financially supported by the National Key Research and Development Program of China (Grant No. 2021YFB2400400), the National Natural Science Foundation of China (Grant Nos. 52171203, 52371214, 52101261, and 52302224), the Natural Science Foundation of Jiangsu Province (Grant Nos. BK20211516 and BK20221179), the Fundamental Research Funds for the Central Universities (Grant No. 2242023K5001), and the Natural Science Foundation of Shandong Province (ZR2023QB119).

Conflict of Interest

The authors declare no conflict of interest.

Data Availability Statement

Research data are not shared.

Keywords

aqueous ammonium-ion batteries, coating layer, enhanced reaction kinetics and cyclic stability, in situ polymer encapsulation, Mn-Prussian blue analogues

Received: July 2, 2024
Revised: August 7, 2024
Published online:

- [1] Z. D. Huang, Y. Hou, T. R. Wang, Y. W. Zhao, G. J. Liang, X. L. Li, Y. Guo, Q. Yang, Z. Chen, Q. Li, L. T. Ma, J. Fan, C. Y. Zhi, *Nat. Commun.* **2022**, *12*, 4885.
- [2] D. Kundu, B. D. Adams, V. Duffort, S. H. Vajargah, L. F. Nazar, *Nat. Energy* **2016**, *1*, 16119.
- [3] H. Dong, O. Tutusaus, Y. L. Liang, Y. Zhang, Z. L. Higgins, W. L. Yang, R. Mohtadi, Y. Yao, *Nat. Energy* **2020**, *5*, 1043.
- [4] A. Ponrouch, C. Frontera, F. Bardé, M. R. Palacin, *Nat. Mater.* **2016**, *15*, 169.
- [5] X. Liu, X. Y. Wang, Y. R. Zhou, B. C. Wang, L. G. Zhao, H. Zheng, J. B. Wang, J. H. Liu, J. Liu, Y. Y. Li, *Adv. Mater.* **2024**, *36*, 2308447.
- [6] L. G. Yue, X. Y. Wang, L. Chen, D. J. Shen, Z. H. Shao, H. Wu, S. F. Xiao, W. Q. Liang, Y. J. Yu, Y. Y. Li, *Energy Environ. Sci.* **2024**, *17*, 1117.
- [7] W. Wang, X. Y. Wang, J. W. Shan, L. G. Yue, Z. H. Shao, L. Chen, D. Z. Lu, Y. Y. Li, *Energy Environ. Sci.* **2023**, *6*, 2669.
- [8] G. J. Liang, F. N. Mo, X. L. Ji, C. Y. Zhi, *Nat. Rev. Mater.* **2021**, *6*, 109.
- [9] Y. Song, Q. Pan, H. Z. Lv, D. Yang, Z. M. Qin, M. Y. Zhang, X. Q. Sun, X. X. Liu, *Angew. Chem., Int. Ed.* **2021**, *60*, 5718.
- [10] S. Dong, W. Shin, H. Jiang, X. Wu, Z. Li, J. Holoubek, W. F. Stickle, B. Key, C. Liu, J. Lu, P. A. Greaney, X. Zhang, X. Ji, *Chem* **2019**, *5*, 1537.
- [11] G. Liang, Y. Wang, Z. Huang, F. Mo, X. Li, Q. Yang, D. Wang, H. Li, S. Chen, C. Zhi, *Adv. Mater.* **2020**, *32*, 1907802.
- [12] X. Wu, Y. Qi, J. J. Hong, Z. Li, A. S. Hernandez, X. Ji, *Angew. Chem., Int. Ed.* **2017**, *56*, 13026.
- [13] H. Li, J. Yang, J. Cheng, T. He, B. Wang, *Nano Energy* **2020**, *68*, 104369.
- [14] A. Simonov, T. D. Baerdemaeker, H. L. B. Boström, M. L. R. Gómez, H. J. Gray, D. Chernyshov, A. Bosak, H. B. Bürgi, A. L. Goodwin, *Nature* **2020**, *578*, 256.
- [15] M. Du, X. Y. Wang, P. B. Geng, Q. Li, Y. J. Gu, Y. An, H. Pang, *Chem. Eng. J.* **2021**, *420*, 130518.
- [16] Y. X. Huang, M. Xie, Z. H. Wang, Y. Jiang, Y. Yao, S. J. Li, Z. H. Li, L. Li, F. Wu, R. J. Chen, *Small* **2018**, *14*, 1801246.
- [17] N. Song, S. Y. Ren, Y. Zhang, C. Wang, X. F. Lu, *Adv. Funct. Mater.* **2022**, *32*, 2204751.
- [18] Y. X. Zeng, J. Z. Xu, Y. Wang, S. Li, D. Y. Luan, X. W. Lou, *Angew. Chem., Int. Ed.* **2022**, *134*, 202212031.
- [19] Y. Shang, X. X. Li, J. J. Song, S. Z. Huang, Z. Yang, Z. C. Xu, H. Y. Yang, *Chem* **2020**, *6*, 1804.
- [20] J. M. Peng, Y. Li, Z. Q. Chen, G. M. Liang, S. J. Hu, T. F. Zhou, F. H. Zheng, Q. C. Pan, H. Q. Wang, Q. Y. Li, J. W. Liu, Z. P. Guo, *ACS Nano* **2021**, *15*, 11607.
- [21] H. B. Yan, S. M. Li, Y. Nan, S. B. Yang, B. Li, *Adv. Energy Mater.* **2021**, *11*, 2100186.
- [22] X. Cheng, F. M. Ran, Y. F. Huang, R. T. Zheng, H. X. Yu, J. Shu, Y. Xie, Y. B. He, *Adv. Funct. Mater.* **2021**, *31*, 2100311.
- [23] Q. Q. Ren, Y. F. Yuan, S. Wang, *ACS Appl. Mater. Interfaces* **2022**, *14*, 23022.

- [24] I. Moez, D. Susanto, W. Chang, H. D. Lim, K. Y. Chung, *Chem. Eng. J.* **2021**, 425, 130547.
- [25] J. J. Wang, J. G. Wang, H. Y. Liu, Z. Y. You, Z. Li, F. Y. Kang, B. Q. Wei, *Adv. Funct. Mater.* **2021**, 31, 2007397.
- [26] F. Zou, H. C. Nallan, A. Dolocan, Q. Xie, J. Y. Li, B. M. Coffey, J. G. Ekerdt, A. Manthiram, *Energy Storage Mater.* **2021**, 43, 499.
- [27] H. H. Diao, M. Y. Jia, N. Zhao, X. X. Guo, *ACS Appl. Mater. Interfaces* **2022**, 14, 24929.
- [28] U. Nisar, N. Muralidharan, R. Essehli, R. Amin, I. Belharouak, *Energy Storage Mater.* **2021**, 38, 309.
- [29] C. J. Zuo, Z. X. Hu, R. Qi, J. J. Liu, Z. B. Li, J. L. Lu, C. Dong, K. Yang, W. Y. Huang, C. Chen, Z. B. Song, S. C. Song, Y. M. Yu, J. X. Zheng, F. Pan, *Adv. Energy Mater.* **2020**, 10, 2000363.
- [30] M. J. Chen, X. Q. Li, Y. J. Yan, Y. T. Yang, Q. J. Xu, H. M. Liu, Y. Y. Xia, *ACS Appl. Mater. Interfaces* **2022**, 14, 1092.
- [31] Y. Zhao, R. K. Zhou, Z. H. Song, X. D. Zhang, T. Zhang, A. B. Zhou, F. Wu, R. J. Chen, L. Li, *Angew. Chem., Int. Ed.* **2022**, 61, 202212231.
- [32] H. C. Guan, R. C. Lian, R. J. Li, J. H. Zhu, Z. X. Zhao, L. Liu, X. L. Chen, C. M. Jiao, S. P. Kuang, *Adv. Funct. Mater.* **2024**, 34, 2313224.
- [33] J. X. Wang, R. S. Wilson, L. Aristilde, *Proc. Natl. Acad. Sci. USA* **2024**, 121, 2316569121.
- [34] S. Rahaman, M. B. Kanakala, M. Waldiya, A. Sadhanala, C. V. Yelamaggad, K. Pandey, *J. Power Sources* **2023**, 564, 232801.
- [35] Y. K. Yi, F. Hai, X. L. Tian, Z. D. Wu, S. T. Zheng, J. Y. Guo, W. T. Chen, W. B. Hua, L. Qu, M. T. Li, *Chem. Eng. J.* **2023**, 466, 143303.
- [36] J. Huang, X. Tang, K. Liu, G. Fang, Z. He, Z. Li, *Mater. Today Energy* **2020**, 17, 100475.
- [37] C. Y. Li, W. Q. Yan, S. S. Liang, P. Wang, J. Wang, L. J. Fu, Y. S. Zhu, Y. H. Chen, Y. P. Wu, W. Huang, *Nanoscale Horiz.* **2019**, 4, 991.
- [38] X. K. Zhang, M. T. Xia, T. T. Liu, N. Peng, H. X. Yu, R. T. Zheng, L. Y. Zhang, M. Shui, J. Shu, *Chem. Eng. J.* **2021**, 421, 127767.
- [39] S. Y. Li, M. T. Xia, C. X. Xiao, X. K. Zhang, H. X. Yu, L. Y. Zhang, J. Shu, *Dalton Trans.* **2021**, 50, 6520.
- [40] H. X. Yu, J. X. Xu, C. C. Deng, M. T. Xia, X. K. Zhang, J. Shu, Z. B. Wang, *ACS Appl. Energy Mater.* **2021**, 4, 9594.
- [41] W. X. Hou, C. Yan, P. R. Shao, K. Dai, J. Yang, *Nanoscale* **2022**, 14, 8501.
- [42] Z. Z. Zhao, W. Zhang, M. Liu, D. Wang, X. Y. Wang, L. R. Zheng, X. Zou, Z. Z. Wang, D. B. Li, K. K. Huang, W. T. Zheng, *Energy Environ. Mater.* **2023**, 6, 12342.
- [43] H. Liu, K. X. Zhang, S. L. Wang, X. Cai, *Small* **2024**, 16, 2310835.
- [44] S. G. Krishnan, H. D. Pham, C. Padwal, H. Weerathunga, X. J. Wang, K. Mahale, D. Dubal, *J. Power Sources* **2023**, 570, 232994.
- [45] W. Yang, L. Xu, W. Luo, M. Huang, K. Fu, R. G. Song, C. H. Han, R. Tu, J. Shi, L. Q. Mai, *Matter* **2023**, 6, 3006.
- [46] Y. L. Wu, S. Y. Dong, N. Lv, Z. K. Xu, R. Q. Ren, G. Y. Zhu, B. L. Huang, Y. Z. Zhang, X. C. Dong, *Small* **2022**, 18, 2204888.
- [47] K. Niu, J. J. Shi, L. Zhang, Y. Yue, S. Y. Mo, S. F. Li, W. B. Li, L. Wen, Y. X. Hou, L. Sun, S. W. Yan, F. Long, Y. H. Gao, *Adv. Sci.* **2024**, 11, 2305524.
- [48] C. Liu, M. X. Li, J. M. Meng, P. Hei, J. Wang, Y. Song, X. X. Liu, *Adv. Funct. Mater.* **2024**, 34, 2310437.
- [49] Y. Z. Huang, L. Xing, S. Pei, W. Zhou, Y. J. Hu, W. N. Deng, L. Chen, H. Zhu, H. Chen, *Trans. Nonferrous Met. Soc. China* **2023**, 33, 3452.
- [50] Q. Liu, F. Ye, K. L. Guan, Y. T. Yang, H. L. Dong, Y. P. Wu, Z. L. Tang, L. F. Hu, *Adv. Energy Mater.* **2023**, 13, 2202908.
- [51] L. Y. Du, S. S. Bi, M. Yang, Z. W. Tie, M. H. Zhang, Z. Q. Niu, *Proc. Natl. Acad. Sci. USA* **2022**, 119, 2214545119.
- [52] D. W. Wang, Z. R. Sun, X. L. Han, *J. Taiwan Inst. Chem. E.* **2023**, 145, 104845.
- [53] D. D. Ling, Q. Wang, G. F. Tian, H. Yu, D. H. Zhang, Q. F. Wang, *ACS Nano* **2023**, 17, 25222.
- [54] F. Y. Xiong, X. L. Liu, C. L. Zuo, X. L. Zhang, T. Yang, B. B. Zhou, G. B. Zhang, S. S. Tan, Q. Y. An, P. K. Chu, *J. Phys. Chem. Lett.* **2024**, 15, 1321.
- [55] M. J. Chen, X. Q. Li, Y. J. Yan, Y. T. Yang, Q. J. Xu, H. Liu, Y. Y. Xia, *ACS Appl. Mater. Interfaces* **2022**, 14, 1092.
- [56] Q. D. Wang, W. Yang, F. Y. Kang, B. H. Li, *Energy Storage Mater.* **2018**, 14, 361.
- [57] M. J. Hou, S. Q. Gong, L. L. Li, J. H. Huang, M. Z. Xu, Z. F. Chen, *Chem Eng J* **2021**, 419, 129575.
- [58] H. D. Zhang, Y. Tian, W. X. Wang, Z. L. Jian, W. Chen, *Angew. Chem., Int. Ed.* **2022**, 61, 202204351.
- [59] D. Yang, Y. Song, M. Y. Zhang, Z. M. Qin, J. Liu, X. X. Liu, *Angew. Chem., Int. Ed.* **2022**, 61, 202207711.